

Interaction-induced interference in the integer quantum Hall effect

I. Sivan,¹ R. Bhattacharyya,¹ H. K. Choi,^{1,2,*} M. Heiblum,^{1,***} D. E. Feldman,³ D. Mahalu,¹ and V. Umansky¹

¹ *Braun Center for Sub-Micron Research, Department of Condensed Matter Physics, Weizmann Institute of Science, Rehovot, Israel 76100*

² *Department of Physics, Research Institute of Physics and Chemistry, Chonbuk National University, Jeonju 54896, Korea*

³ *Department of Physics, Brown University, Providence, Rhode Island 02912, USA*

ABSTRACT

A recent experiment with a Fabry–Perot interferometer (FPI), operating in the integer quantum Hall effect regime, revealed that the period of the Aharonov–Bohm (AB) oscillations drops by a half at bulk fillings $v_B > 2.5$, accompanied by an interfering charge $e^* = 2e$. Although charge e is observed when the visibility is low, the single-particle interference is invariably fully dephased. Counterintuitively, the interference periodicity is determined by the area enclosed by the second-inner edge channel, separating the $v = 1$ and $v = 2$ regions, and not by the area within the outermost interfering channel. Such pairing is not observed in a Mach–Zehnder interferometer (MZI). A combination of an MZI and an FPI elucidates the role of the second-inner edge mode, as well as the formation of paired–electrons quasiparticles. The results suggest that a neutral chiral edge mode plays a crucial role in the pairing phenomenon. Our findings reveal that the observed pairing is not a curious isolated phenomenon, but one of many manifestations of unexpected edge physics in the quantum Hall regime.

I. INTRODUCTION

Electron interferometry has played a significant role in the investigation of the foundations of quantum mechanics. As fabrication techniques improve, and novel materials develop, interferometers are realized in numerous mesoscopic systems, such as quantum Hall systems [1–4], nanowires [5], carbon nanotubes [6,7], and graphene [8,9]. In many experiments, newly developed electronic interferometers have revealed unexpected phenomena mostly because of electron interaction [10–14].

The quantum Hall effect (QHE) provides particularly attractive settings for interference experiments, since it allows an easy control of electron trajectories via the chiral edge channels. Interferometry in the fractional QHE, which is not observed yet, is particularly important because it is expected to reveal the fractional statistics of the fractionally charged quasiparticles [15–20]. However, the easy-to-access integer QHE, still does not cease to surprise us [14].

Our recent unexpected findings involved Aharonov–Bohm (AB) interference in a screened Fabry–Perot interferometer (FPI). At bulk fillings $\nu_B \geq 2.5$, we reproducibly observed the following: (i) half periodicity in the AB flux ϕ with a period $\phi_0^* = \frac{\hbar}{2e}$; (ii) charge $e^* \sim 2e$ of interfering particles, where e is the electron charge; and (iii) no interference at all when the second-inner edge channel, separating the $\nu = 1$ and $\nu = 2$ regions, is grounded (and not the outermost interfering channel). Similar inter-mode correlations have not been observed at $\nu_B \leq 2.5$. Moreover, the flux periodicity was the ubiquitous flux quantum $\phi_0 = \frac{\hbar}{e}$ and the interfering charge was e . In this study, we expand our initial measurements, focusing on the collective effects owing to the edge channel interaction. We suggest that a neutral mode plays a special role in the interferometry.

II. BACKGROUND

A. Measurement setup

The FPIs were realized in a high-mobility 2D electron gas (2DEG) that was embedded in MBE-grown GaAs/AlGaAs heterostructures. By employing the general fabrication process, the FPI was realized with two quantum point contacts (QPCs) that serve as “beam splitters”. Typical Coulomb blockade physics was suppressed in favor

of coherent AB interference with two different implementations (Figs. 1(a) and 1(b)) [10,14]. In Fig. 1(b), a metallic (Ti–Au) top-gate covered the entire area of the FPI and provided intra-channel screening, whereas, in Fig. 1(a), a small grounded Ohmic contact (Ni–Ge–Au) was placed in the interior of the FPI, allowing draining electrons from the interior of the FPI. Although the two configurations behave similarly, the latter allows more flexibility in the fabrication of different devices. In all the FPIs, the outermost edge channel interfered with itself (red lines in Figs. 1(c) and 1(d)), whereas the inner edge channels (blue and green lines in Figs. 1(c) and 1(d)) were trapped inside the FPI. In a few configurations, another “center-QPC” was placed within the FPI along the path of the edge channels, thus allowing the deflection of each channel individually from its original path (Fig. 1(d)). An AC signal (1 μ V RMS @ 800 kHz) was applied at the Source. The Drain voltage (proportional to the transmission of the FPI) was filtered with an LC circuit and amplified by an amplification chain (a cold homemade preamplifier with small signal gain $G = 11$, followed by a room temperature amplifier, NF SA-220F5, with gain 200).

B. Interference in FPI

The interference in an FPI at bulk fillings $\nu_B = 2$ and $\nu_B = 3$, with area $A_{FP} = 2\mu\text{m}^2$, is plotted as a function of magnetic field B and modulation gate voltage V_{MG} , in Fig. 2. At $\nu_B = 2$, the AB frequency corresponds to $\frac{\phi_0}{\Delta B} = 2.05 \mu\text{m}^2$, which is in striking contrast to that at $\nu_B = 3$ where it corresponds to $\frac{\phi_0}{\Delta B} = 4.1 \mu\text{m}^2$. These two frequencies exhibit similar visibilities, with the latter remaining fairly constant throughout the region $2.5 \leq \nu_B \leq 4.5$ [14].

One may wish to explain the “frequency doubling” by assuming the preferred even number of winding trajectories; however, this would lead to a considerably lower visibility. Moreover, and most importantly, the doubling of the interfering charge at $\nu_B = 3$, $e^* = 2e$ (determined by shot noise measurements [14]), also excludes this scenario. Note that such pairing is not observed in a Mach–Zehnder interferometer (MZI) (Appendix B).

C. Quasiparticle charge and visibility

As the pairing phenomenon, with $e^* = 2e$, was tightly tied to double the frequency of the AB oscillations, the charge was measured as a function of visibility. Visibility was

gradually suppressed by the following: (i) directing the second-inner edge channel to the internal grounded contact, thereby dephasing the FPI (see also below) [14]; (ii) opening one of the QPCs that form the FPI by increasing its transmission and lowering its reflection. In both the cases, the visibility gradually reduced, and similar trend was noticed in the charge of the quasiparticles (see Appendix C). The quasiparticle charge appears to follow qualitatively the visibility of the interference, reaching $e^*=2e$ when the visibility reaches some 45%. The non-quantized charge is a statistical average between the two quantized values, e and $2e$ [21]. Yet, the AB flux periodicity remains $h/2e$, all along with no sign of the h/e periodicity. The only way to understand this contradiction is to assume that the single electrons are fully dephased in the pairing regime.

III. ROLE OF THE SECOND CHANNEL

As it is expected that electron interactions between different edge modes are responsible for the pairing phenomenon, we studied, in detail, the role of the second edge channel that separates the filling factors 1 and 2.

A. Grounding the second channel

By employing the FPI shown in Fig. 1(d), one can reflect the edge channels one by one toward the grounded center Ohmic contact with the center-QPC (colored green). First, at $\nu_B = 2$, the transmitted current through the FPI and the visibility quench simultaneously and abruptly when the outermost interfering channel is fully dephased (Figs. 3(a) and 3(c)). Grounding only the second-inner channel had no added effect on the visibility or the current of the interfering channel. Repeating the same experiment at $\nu_B \sim 3$ led to a dramatically different effect. The interference fully quenched when the second-inner channel was grounded; however, as expected, it did not change the traversing current carried by the outermost channel (Figs. 3(b) and 3(d)]. Evidently, the coherence of the second-inner channel is indispensable for the $\frac{h}{2e}$ flux periodicity.

B. Dependence on the AB flux confined by the second-inner channel

A different implementation of the FPI, which included an added island in its interior, allowed channels to change their enclosed AB area by A_{island} , if “QPC-down” was pinched and “QPC-top” remained open (Fig. 4). In a modified implementation, the

“QPC-down” was replaced by a “long constriction” (Appendix D). A trajectory around the island accumulates an AB phase $\delta\varphi_{AB} = 2\pi \cdot \frac{(n \cdot A_{FP} - m \cdot A_{island})\delta B}{\phi_0}$, where n and m represent the numbers of windings that an electron makes around the FPI and around the island, respectively. Hence, the two fundamental periods in B are ϕ_0/A_{FP} and $\phi_0/(A_{FP} - A_{island})$, with the visibilities determined by the transmissions of the QPCs, were observed.

At $v_B = 2$, with “QPC-down” in its two configurations, a clear transition is observed in the AB frequency from $\frac{\phi_0}{\Delta B} = A_{FP} = 10.3 \mu\text{m}^2$, when “QPC-down” was fully open, to $\frac{\phi_0}{\Delta B} = A_{FP} - A_{island} = 7.6 \mu\text{m}^2$, when “QPC-down” was fully pinched (Fig. 5). Evidently, the path taken by the second-inner channel has no effect on the AB interference (Appendix E).

However, at $v_B = 3$, the transition between the two AB frequencies took place when the second-inner channel was fully reflected to go around the island while the outermost interfering channel remained intact. Here, the AB frequencies switched from $\frac{\phi_0}{\Delta B} = 23.2 \mu\text{m}^2$ to $\frac{\phi_0}{\Delta B} = 17.8 \mu\text{m}^2$ (Figs. 5(d)–5(f) and Appendix E). Note that the innermost (third inner) edge channel was never observed to play a direct role in the interference; however, it was crucial for the observation of the pairing. Its role was likely to screen the two outer channels from the bulk.

On the other hand, employing the “long constriction” for the “QPC-down”, led to a markedly different effect at $v_B = 3$ (Figs. 6(a) and 6(b), Appendix E). While the AB frequencies switched again from $\frac{\phi_0}{\Delta B} = 23.2 \mu\text{m}^2$ for a fully open to $\frac{\phi_0}{\Delta B} = 17.8 \mu\text{m}^2$ for a fully pinched “long constriction,” a transition region appeared, corresponding to the fully reflected second channel (the outermost channel remained unperturbed), with a low visibility. This effect suggests the formation of a compound quasiparticle owing to the interaction between the two outer channels. Apparently, its transmission coefficient through the “long constriction” is smaller than the transmission coefficient in a narrow QPC.

C. Direct test of the interaction between the two outer edge channels

In any model that explains the pairing phenomenon, the Coulomb interaction between the two outer channels must play a crucial role.

An FPI was placed in one arm of an MZI [1,22]. The MZI was designed to interfere only the outermost edge channel. We compared two regimes of the FPI: one, when the outermost channel passed freely through the FPI; and the other, when the FPI partitioned the outmost channel - thus interfering inside the FPI (Fig. 7). Note, that outside the FPI the second and third channels were fully reflected from the FPI, while within the FPI they were fully trapped.

At $\nu_B = 2$, with the outermost channel passing freely through the FPI, a single frequency, corresponding to $\frac{\phi_0}{\Delta B} = 14.39 \mu\text{m}^2 = A_{MZ}$, is observed (Figs. 8(a) & 8(b)). At $\nu_B = 3$, the situation is entirely different. Two frequencies appear: one corresponding to A_{MZ} , and another corresponding to $\phi_0/\Delta B = A_{MZ} - A_{FP}$ (Fig. 8(d)). These frequencies persist with a nearly constant visibility from a nearly fully transmitted to a strongly pinched outermost channel in the FPI.

This phenomenon can be understood as follows. Since the second-inner channel is confined, its area decreases with increasing magnetic field in order to keep the filling factor fixed (say, with N electrons). The outermost channel also moves inwards, changing its accumulated phase in the FPI. Eventually, the area, enclosed by the second-inner channel abruptly increases as a new electron is added (occupation increases to $N+1$) [4]. Appendix F shows how such breathing introduces an additional AB frequency. Moreover, at the degeneracy point of occupations N and $N+1$, the area enclosed by the second-inner channel fluctuates, and the AB phase gained by the outermost channel fluctuates between zero and π due to the Friedel sum rule [27]; leading to dephasing exactly at the degeneracy point. As the FPI pinches, the lifetime of the second-inner channel increases and the degeneracy region gets sharper. Higher orders of the AB frequency, represented by the area A_{FP} appear (see details in Appendix F). Evidently, this signature of the interaction between the two outer channels cannot be transparent in the stand-alone FPI.

IV. IS PAIRING A SINGLE ELECTRON PHENOMENON?

Employing the above configuration of MZI + FPI, one can examine whether the observed pairing results from a single-particle effect, or due to the formation of a new double-charge quasiparticle.

In the single-particle picture, the transmission amplitude of the combined MZI–FPI interferometer is

$$\tau_{MZI+FPI} = t^2 + r^2 e^{i\varphi_{MZI}} \cdot \tau^2 \sum_{n=0}^{\infty} (\rho^2 e^{-i\varphi_{FPI}})^n, \quad (1)$$

where t (τ) and r (ρ) are the (real) transmission and reflection amplitudes of the QPCs (both with a similar tuning) forming the MZI (FPI), respectively, and $n = 0, 1, 2, \dots$ denotes the number of windings in the FPI. The accumulated AB phase in the FPI, φ_{FPI} , is subtracted from that of the MZI, φ_{MZI} , owing to the opposite chirality of the channels with respect to that in the MZI. The transmission probability $T = |\tau_{MZI+FPI}|^2$ can be decomposed into three terms (plus a flux-independent constant):

$$T_{MZI} = \tau^2 C_1 \cos \varphi_{MZI}, \quad (2a)$$

$$T_{FPI} = r^4 \sum_{n=1}^{\infty} D_n \cos(n\varphi_{FPI}), \quad (2b)$$

$$T_{MZI+FPI} = \sum_{n=1}^{\infty} E_n \cos(\varphi_{MZI} - n\varphi_{FPI}), \quad (2c)$$

where T_{MZI} and T_{FPI} are the transmission probabilities (up to a constants) of each interferometer independently. Naturally, in a single-particle picture, $T_{MZI+FPI}$ should oscillate with the AB frequencies $\frac{\phi_0}{\Delta_B} = A_{MZ} - nA_{FP}$, as well as the oscillation frequency of the transmission coefficient of a stand-alone FPI, $\frac{\phi_0}{\Delta_B} = nA_{FP}$, which modulates the transmission of the MZI path passing through the FPI.

At $v_B = 2$, with the FPI being gradually pinched, a frequency corresponding to $\frac{\phi_0}{\Delta_B} = 2.16 \mu\text{m}^2 = A_{FP}$ appears first (Fig. 8(a)). With further pinching, one can see higher harmonics, $\frac{\phi_0}{\Delta_B} = 2A_{FP}, 3A_{FP}, \dots$, as well as those of the combined setup, $\frac{\phi_0}{\Delta_B} = A_{MZ} - A_{FP}, A_{MZ} - 2A_{FP}, A_{MZ} - 3A_{FP}$. These are the expected frequencies, alluded to above.

At $v_B = 3$, the measurements do not agree with single-particle interference (Fig. 8(d)). Trivially, the transmission of the MZI path through the FPI oscillates with the corresponding areas $\frac{\phi_0}{\Delta_B} = 2A_{FP}$ and $4A_{FP}$. This is a non-coherent effect. As discussed above, the frequency component proportional to A_{MZ} is due to MZI electrons passing the FPI without interfering, while the component $A_{MZ} - A_{FP}$ was discussed above. These frequencies do not result from interference in the FPI, as they are nearly independent on the pinching of the FPI. The higher harmonic, related to $A_{MZ} - 2A_{FP}$, becomes stronger with pinching, as expected (see above and Appendix

F). Indeed, the paired electrons quasiparticles do not interfere with the electrons traverse the other path of the MZI.

V. DISCUSSION

From its discovery, the QHE has been an extraordinary rich and exciting field of research. Some of its developments led to novel ideas and advances well beyond the QHE physics, such as the discovery of topological insulators [23,24] and the connection of the QHE physics with knot theory [25]. Moreover, it is broadly recognized that the fractional QHE itself is far from being fully understood. In this paper, we show that even the seemingly simpler integer QHE remains a broadly open field for research.

An obvious question is whether the pairing phenomenon described in some details in this study is an isolated puzzle or a part of a broader set of phenomena. With this question in mind, we examined a series of interference structures beyond the simplest FPI setup. With only the outermost channel (lowest spin-split Landau level) interfering, we considered a set of modified FPIs: an MZI that can be smoothly converted to an FPI (Appendix B) and an FPI inserted in one of the two paths of a MZI. In all these structures, the observations were new and surprising. The most significant observation was the importance of the second-inner edge channel, which dictated the interference periodicity and the coherence of the interfering channel.

While not having a detailed model for the observed pairing, one can envision the following scenario, which may explain the dephasing process but not the $2e$ charge of the interfering quasiparticle. Let us look at the configurations where the second-inner channel encloses a different AB area than that of the outermost channel (Figs. 4 and 9(a)), and its grounding leads to dephasing of the outermost interfering channel (Fig. 1(d)). Inter-channel correlations between the outer two channels can be modeled in the following manner (Fig. 9): Particle A with charge $-q$ moves along the outermost interfering channel and induces a screening charge distribution in the second channel. We depict the distribution as a combination of two charged objects B and C, with B carrying charge $+q$, compensating the charge $-q$ of C (Fig. 9(b)). Reaching the narrow QPC constriction, the neutral excitation A–B, seeing a lower barrier than that for the charged excitation, crosses the pinched QPC (Fig. 9(c)). The neutral excitation accumulates a null AB phase in its path, while the AB phase is

determined by particle C that follows the inner channel trajectory that is diverted to go around the island ([Fig. 9(c)]). This accounts for the experimentally observed dominance of the second edge channel. On the other hand, replacing the narrow QPC constriction with a “long constriction”, which diverts the neutral mode as well as particle C to go around the island, quenches the interference altogether. Apparently, the breakdown (as the outermost channel fully transmits at the constriction) and recreation of the composite excitations on the two sides of the “long constriction” may introduce an arbitrary phase to the outermost channel, thus resulting in dephasing.

Our results demonstrate that a complete explanation of the pairing phenomenon should satisfy a considerable number of experimental constraints. However, as it is clear that the electron interactions are a key ingredient of the FQHE, our results reveal that the same is true for the IQHE.

ACKNOWLEDGMENTS

M. H. acknowledges the partial support of the Israeli Science Foundation, Grant No. ISF-459/16 (ISF), the Minerva foundation, the US–Israel Bi-National Science Foundation (BSF), The German Israeli Foundation (GIF), and the European Research Council under the European Community’s Seventh Framework Program (FP7/2007-2013)/ERC Grant Agreement No. 227716. H. K. C. was supported by Korea NRF (Grant No. 2017R1C1B3004301 and No. 2017R1A5A1003375). D. E. F. acknowledges the hospitality of the Weizmann Institute. D. E. F’s research was supported in part by the National Science Foundation under Grant No. DMR-1607451.

* hkchoi@jbnu.ac.kr

** moty.heiblum@weizmann.ac.il

APPENDIX A: NON-INTERACTING FPI

The theory of a non-interacting FPI is well established. The AB phase $\delta\varphi_{AB} = 2\pi\frac{\delta\phi_{FPI}}{\phi_0^*}$ with $\delta\phi_{FPI} = A\delta B + B\delta A$, where A is the area of the device and B is the magnetic field. This phase determines the transmission amplitude τ_{FPI} ,

$$\tau_{FPI} = t^2 \sum_{n=0}^{\infty} (r^2 e^{i\delta\varphi_{AB}})^n = \frac{t^2}{1-r^2 e^{i\delta\varphi_{AB}}}, \quad (\text{A1})$$

where $t = t_L = t_R$ and $r = r_L = r_R$ are the transmission and reflection amplitudes of the left and right QPCs. To the first order in $|r|^2 \ll 1$, the transmission coefficient is $T_{FPI} = |\tau_{FPI}|^2 = |t^2(1 + r^2 e^{i\delta\varphi_{AB}})|^2$. This picture holds for the h/e regime at $v_B < 2.5$.

APPENDIX B: COMBINED MZI–FPI DEVICE

A similar pairing phenomenon to the one observed in the FPI was never observed in an MZI. Indeed, an MZI is topologically different from an FPI: MZI contains a drain inside the interferometer. This does not allow confined inner edge channels in the device. It is possible to construct a structure that allows a smooth transition between the two interferometers, as shown in Fig. 10. Here, two additional QPCs were added to the MZI (middle-QPC, marked blue, and top-QPC, marked green). When the two QPCs are fully open, the device functions as an MZI with the area A_{MZ} ; however, when the two QPCs are pinched, it functions as an FPI with the area A_{FP} . We study the evolution to the pairing regime during a gradual transition from one interferometer to the other.

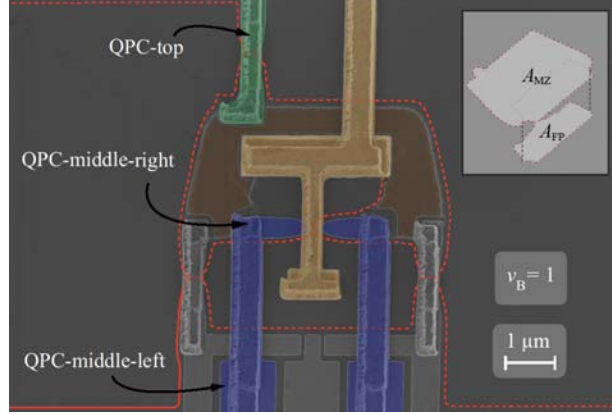


FIG. 10. SEM image of combined Mach–Zehnder and Fabry–Perot device. The device allows a transition from operating as an MZI to operating as an FPI. Edge channels are depicted for the bulk filling factor $\nu_B = 1$ (red lines) for simplicity. At higher fillings, additional channels appear, as shown in Fig. 1. Partitioned current is denoted by dashed lines. There are two Ohmic contacts connected via an air bridge (gold, false color). They are grounded together via a second air bridge. The device can be regarded as an MZI with two additional QPCs: middle-QPC (blue, false color) and top-QPC (green, false color). When the two QPCs are fully open, the device functions as an MZI with the area A_{MZ} ; however, when the two QPCs are fully closed, it functions as an FPI with the area A_{FP} . The gradual transition from one interferometer to the other is studied in Fig. 11.

The AB frequency of the MZI configuration at $\nu_B = 2$, corresponding to the area $A_{MZ} = \frac{\phi_0}{\Delta B} = 21.3 \mu\text{m}^2$, is depicted in Fig. 11(a) (lowest plot, light blue). Interference is not observed for a fully pinched middle-QPC because the reflection from the structure is impossible (not shown). However, as middle-QPC gradually pinches (toward the upper plots in red), additional AB frequencies appear. Prominent ones correspond to the FPI area $A_{FP} = \phi_0/\Delta B = 5.7 \mu\text{m}^2$, as well as to the sum and difference of the two areas: $27 \mu\text{m}^2$ and $15.3 \mu\text{m}^2$.

At $\nu_B = 3$, the frequency in the MZI configuration (Fig. 11(b), lowest plot, blue) is nearly identical to that in Fig. 11(a). As middle-QPC pinches, the double frequency of the FPI, corresponding to $2A_{FP} = 11.4 \mu\text{m}^2$, emerges. In contrast to $\nu_B = 2$, when the FPI forms (middle graph, purple) and the $2A_{FP}$ component increases, the $A_{MZ} = 21.3 \mu\text{m}^2$ component decreases substantially. This suggests the dephasing of the A_{MZ} component when that of the paired electrons in the FPI increases. Moreover, while at $\nu_B = 2$ the frequencies $\frac{\phi_0}{\Delta B} = A_{MZ} \pm A_{FP}$ appear, at

$v_B = 3$ only a weak high band $A_{MZ} + A_{FP}$ is apparent. Clearly, by pairing with $\frac{\phi_0}{\Delta B} = 2A_{MZ}$, frequency is not observed.

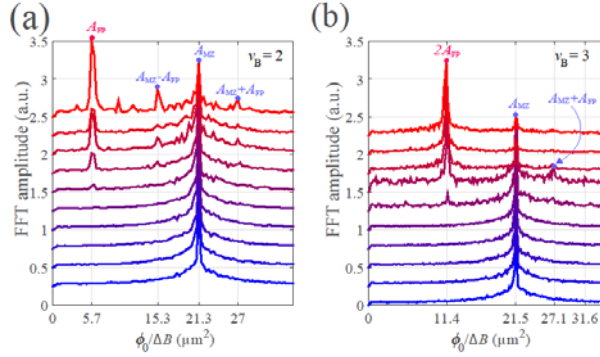


FIG. 11. Effect of opening Fabry-Perot's QPCs on oscillation frequencies, measured using the device shown in Fig. 10. Measurements at $v_B = 2$. Each vertical line is the fast Fourier transform of AB interference oscillations measured as a function of the magnetic field δB for a particular value of the FPI's transmission coefficient. Measurements were performed from the full transmission of the outermost edge channel (lowest graph, blue) to its very low transmission, $t \ll 1$, (highest graph, red). The MZI's QPCs partition the outermost edge channel. (b) Similar measurements to (a), but at $v_B = 3$.

APPENDIX C: EVOLUTION OF $2e$ CHARGE ACCORDING TO THE INTERFERENCE VISIBILITY IN THE FPI

We studied the dependence of quasiparticle charge on the visibility of the FPI at $v_B = 3$. In this experiment, the left-QPC of the FPI is set to be a fixed transmission, t_L , and the transmission of the right-QPC of the FPI, t_R , is varied from zero to one for the outermost edge channel. The visibility of interference and the quasiparticle charge via shot noise were measured, at the same values of t_R , in two separate experiments.

As the doubling of the charge, which is extracted from shot noise measurements [26–29], cannot be easily understood (in any of the proposed models), the charge was verified by employing a few versions of the standard non-interacting expression for the spectral density of the shot noise. An expression that takes into account “bunching” of charge in the partitioning process, where the incoming quasiparticles’ charge is smaller than that of the partitioned ones, is relevant to this phenomenon [30,31]: $S_{\text{shot noise}} = 2e^*It\left(1 - \frac{te}{e^*}\right)L(e^*, V, T)$, where I is the impinging current at the FPI, t is the total transmission through FPI, e^* is the charge

of partitioned quasiparticles, V is the bias voltage, T the temperature, and $L(e^*, V, T)$ is the temperature-dependent Langevin function $L(e^*, V, T) = \coth\left(\frac{e^*V}{2k_B T}\right) - \frac{2k_B T}{e^*V}$.

Fig. 12 shows that the interfering charge, e^* , becomes close to $2e$ when the visibility is at highest; whereas, it shows charge $e^* = e$ when the visibility goes to zero, and $e \leq e^* < 2e$ elsewhere. Moreover, the evolution of the quasiparticle charge follows qualitatively similar to the evolution of the visibility of interference. The charge was not measured for considerably small transmission through the FPI as the shot noise curve fitting becomes unreliable in such cases.

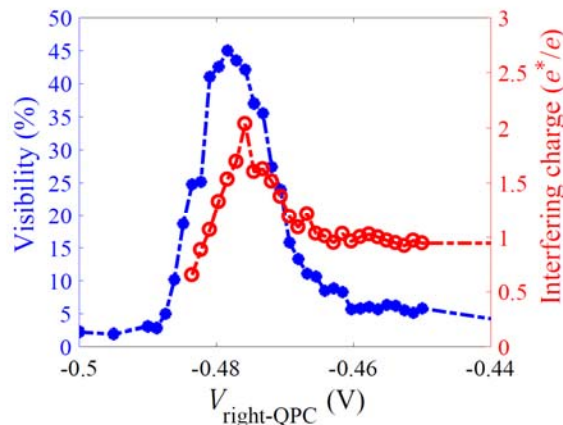


FIG. 12. The dependence of the quasiparticle charge on the visibility as one of the QPC's gradually opened at $v_B = 3$. The blue curve shows the evolution of the interference visibility as a function of t_R (in terms of the voltage on the right-QPC) for a fixed t_L . With the same QPC transmissions, the quasiparticle charge in the FPI is measured via shot noise (red). Notably, the evolution of the interfering charge follows the evolution of the visibility to a good agreement.

APPENDIX D: EMPLOYING EXTENDED CONSTRICTION

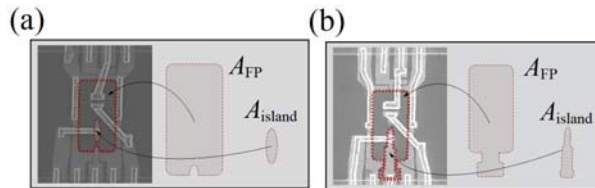


FIG. 13. Top-view SEM images of Fabry-Perot interferometer with an “island” in its center. (a) Top-view SEM image of the device shown in Fig. 4 alongside with illustrations of A_{FPI} , the FPI's area, and

A_{island} , the island's area. (b) Top-view SEM image of a device similar to the one in (a) but with an extended constriction between the island and the edge of the FPI. As discussed in the main text, the effect of reflecting edge channels one by one from the interferometer's edge to the island differs for the device shown in (a and b).

APPENDIX E: THE EFFECT OF SELECTIVE REFLECTION OF EDGE CHANNELS INTO THE GROUND

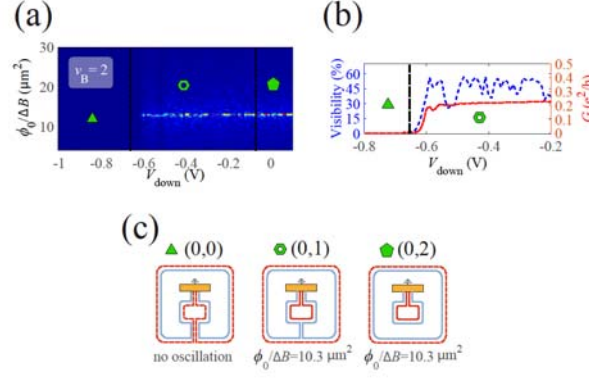


FIG. 14. Evolution of the interference area as QPC-down is pinched, measured with the device shown in Fig. 4(a) at $v_B = 2$ with fully closed QPC-up. (a) 2D plot of the fast Fourier transform of AB interference oscillations as a function of the magnetic field δB for a particular value of V_{down} that determines the transmission of QPC-down. QPC-up is maintained fully closed at all times. (b) Conductance (extracted from the AB interference) and visibility (extracted from (a)) are plotted as functions of V_{down} for fully open QPC-up. (c) Illustrations of different configurations with QPC-down reflecting both edge channels (left), only the outermost edge channel (middle), and none of the edge channels (right). Above each illustration, we show as (v_{up}, v_{down}) the numbers of fully transmitted channels in QPC-down, v_{down} , and in QPC-up, v_{up} .

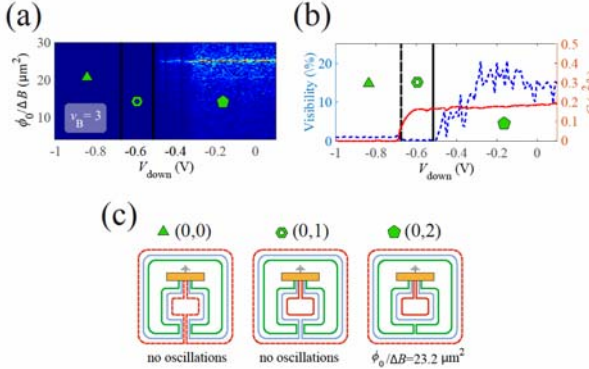


FIG. 15. Evolution of the interference area as QPC-down is pinched, measured using the device shown in Fig. 4(a) at $v_B = 3$ with QPC-up fully closed. (a) Measurements at $v_B = 3$. 2D plot of the fast Fourier transform of AB interference oscillations as a function of the magnetic field δB for a particular value of V_{down} that determines the transmission of QPC-down. QPC-up is maintained fully closed at all times. (b) Conductance (extracted from the AB interference, red) and visibility (extracted from (a), blue) are plotted as functions of V_{down} for fully closed QPC-up. (c) Illustrations of different configurations with QPC-down reflecting both edge channels (left), only the outermost edge channel (middle), and none of the edge channels (right). Above each illustration, we show as (v_{up}, v_{down}) the numbers of fully transmitted channels in QPC-down, v_{down} , and in QPC-up, v_{up} .

APPENDIX F: SIMULATION FOR THE CONDUCTANCE OF THE MZI+FPI DEVICE

We observe the frequency $A_{MZ} - A_{FP}$ in the configuration of MZI + FPI, shown in Fig. 8(d) in the main text, which appears when the FPI fully transmits the outermost channel while maintaining the second channel confined. The frequency persists as the FPI is pinched. This frequency can be derived from the Friedel sum rule [32], which connects the scattering phase with the electron occupancy. In our device, an electron added to the FPI, formed by the second edge channel, is screened by electrons from the outermost edge channel. While the screening electrons from an arm of the MZI pass the FPI without backscattering, they acquire a scattering phase that depends on the electron number in the FPI. Consequently, the MZI is dephased periodically at every resonance of the FPI owing to the degeneracy [22] of the FPI state at the resonance. We show a simple simulation that explains the above physics in Fig. 16. For simplicity, we use two parameters: 1. The phase shift of the MZI $\Delta\varphi_{MZI} = \pi$ at the FPI's resonance; 2. As the shapes of the visibility dips are the same as those of the conductance peaks owing to the transport through the second edge of the FPI, we model the visibility as a function of the FPI transmission T_{FPI} as shown below [22]:

$$T_{FPI} = \left| t^2 \sum_{n=0}^{\infty} (r^2 e^{i\delta\varphi_{FPI}})^n \right|^2 = \left| \frac{t^2}{1 - r^2 e^{i\delta\varphi_{FPI}}} \right|^2, \text{Visibility} = 1 - T_{FPI}. \quad (F1)$$

Here, we took the transmission $t = 0.75$. This is because considering a lower transmission does not change physics, just produces more sub-harmonics.

Our model appears to apply at both $v_B = 2$ and $v_B = 3$, yet the observed behavior is different in the two cases. Apparently, the pairing physics, which is present only at $v_B = 3$, is essential. We do not know yet how to incorporate it in our model.

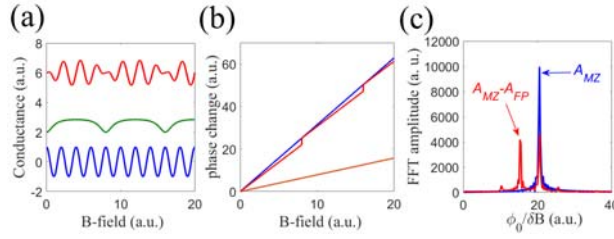


FIG. 16. Simulation for the conductance through the device in Fig. 7 in the main text. (a) AB oscillations of an MZI (blue) and of an MZI with a quantum dot (QD, equivalent with FPI here) formed by the adjacent second edge channel (red) as functions of the magnetic field. The QD causes a phase shift of the MZI by π when the number of electrons changes in QD at resonance, resulting in the dephasing of the MZI (red) as shown in its visibility (green). (b) Phase change of the MZI without QD (blue) and with QD (red). Brown plot is the phase change of QD. (c) Fast Fourier transform of the AB oscillations of (a).

References

- [1] Y. Ji, Y. Chung, D. Sprinzak, M. Heiblum, and D. Mahalu, *Nature* **422**, 415 (2003).
- [2] I. Neder, N. Ofek, Y. Chung, M. Heiblum, D. Mahalu, and V. Umansky, *Nature* **448**, 333 (2007).
- [3] E. Weisz, H. K. Choi, I. Sivan, M. Heiblum, Y. Gefen, D. Mahalu, and V. Umansky, *Science* **344**, 1363 (2014).
- [4] I. Sivan, H. K. Choi, J. Park, A. Rosenblatt, Y. Gefen, D. Mahalu, and V. Umansky, *Nat. Commun.* **7**, 12184 (2016).
- [5] S. S. Hong, Y. Zhang, J. J. Cha, X. L. Qi, and Y. Cui, *Nano Lett.* **14**, 2815 (2014).
- [6] A. Bachtold, C. Strunk, J. J.-P. Salvetat, J.-M. Bonard, L. Forro, T. Nussbaumer, and C. Schonenberger, *Nature* **397**, 673 (1999).
- [7] W. Liang, M. Bockrath, D. Bozovic, J. H. Hafner, M. Tinkham, and H. Park, *Nature* **411**, 665 (2001).
- [8] L. C. Campos, A. F. Young, K. Surakitbovorn, K. Watanabe, T. Taniguchi, and P. Jarillo-Herrero, *Nat. Commun.* **3**, 1239 (2012).

- [9] D. S. Wei, T. Van Der Sar, K. Watanabe, T. Taniguchi, B. I. Halperin, and A. Yacoby, arXiv:1703.00110v1 (2017).
- [10] N. Ofek, A. Bid, M. Heiblum, A. Stern, V. Umansky, and D. Mahalu, Proc. Natl. Acad. Sci. U. S. A. **107**, 5276 (2010).
- [11] Y. Zhang, D. McClure, E. Levenson-Falk, C. Marcus, L. Pfeiffer, and K. West, Phys. Rev. B **79**, 241304 (2009).
- [12] A. Yacoby, M. Heiblum, V. Umansky, H. Shtrikman, and D. Mahalu, Phys. Rev. Lett. **73**, 3149 (1994).
- [13] I. Neder, M. Heiblum, Y. Levinson, D. Mahalu, and V. Umansky, Phys. Rev. Lett. **96**, 16804 (2006).
- [14] H. K. Choi, I. Sivan, A. Rosenblatt, M. Heiblum, V. Umansky, and D. Mahalu, Nat. Commun. **6**, 7435 (2015).
- [15] C. de C. Chamon, D. E. Freed, S. a. Kivelson, S. L. Sondhi, and X. G. Wen, Phys. Rev. B **55**, 2331 (1997).
- [16] A. Stern and B. Halperin, Phys. Rev. Lett. **96**, 16802 (2006).
- [17] P. Bonderson, A. Kitaev, and K. Shtengel, Phys. Rev. Lett. **96**, 16803 (2006).
- [18] K. T. Law, D. E. Feldman, and Y. Gefen, Phys. Rev. B **74**, 45319 (2006).
- [19] D. E. Feldman and A. Kitaev, Phys. Rev. Lett. **97**, 186803 (2006).
- [20] D. E. Feldman, Y. Gefen, A. Kitaev, K. T. Law, and A. Stern, Phys. Rev. B **76**, 85333 (2007).
- [21] D. E. Feldman and M. Heiblum, Phys. Rev. B **95**, 115308 (2017).
- [22] E. Weisz, H. K. Choi, M. Heiblum, Y. Gefen, V. Umansky, and D. Mahalu, Phys. Rev. Lett. **109**, 250401 (2012).
- [23] M. Z. Hasan and C. L. Kane, Rev. Mod. Phys. **82**, 3045 (2010).
- [24] X.-L. Qi and S.-C. Zhang, Rev. Mod. Phys. **83**, 1057 (2011).
- [25] C. Nayak, S. H. Simon, A. Stern, M. Freedman, and S. Das Sarma, Rev. Mod. Phys. **80**, 1083 (2007).

- [26] R. De-Picciotto, M. Reznikov, M. Heiblum, V. Umansky, G. Bunin, and D. Mahalu, *Nature* **389**, 162 (1997).
- [27] L. Saminadayar, D. Glattli, Y. Jin, and B. Etienne, *Phys. Rev. Lett.* **79**, 2526 (1997).
- [28] M. Dolev, M. Heiblum, V. Umansky, A. Stern, and D. Mahalu, *Nature* **452**, 829 (2008).
- [29] M. Büttiker, *Phys. Rev. B* **46**, 12485 (1992).
- [30] T. Griffiths, E. Comforti, M. Heiblum, A. Stern, and V. Umansky, *Phys. Rev. Lett.* **85**, 3918 (2000).
- [31] M. Heiblum, *Phys. Status Solidi* **243**, 3604 (2006).
- [32] T. Taniguchi and M. Büttiker, *Phys. Rev. B* **60**, 13814 (1999).

Figures

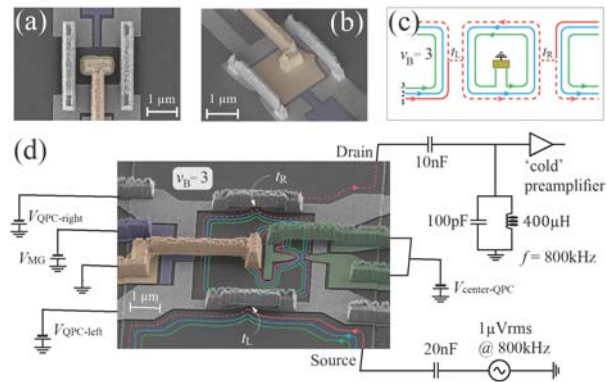


FIG. 1. SEM images of Fabry–Perot interferometers and illustrations of the electronic setup and the chiral edge channels. (a) SEM image of a Fabry–Perot interferometer with a grounded Ohmic contact in its center (gold, false color) aimed at suppressing Coulomb interactions; such devices show AB interference. (b) SEM image of FPI covered with a grounded top-gate (gold, false color), aimed at suppressing Coulomb interactions. (c) Illustration of the chiral edge channels in our setup at $v_B=3$. The red, blue, and green lines represent the outermost, the second, and the third edge channels, respectively. The dashed lines represent current partitioned by a QPC. In the case presented, the outermost edge channel is partitioned in both QPCs. The Ohmic contact is illustrated in the middle of the setup, and the third edge channel is reflected into it by the center-QPC seen in (d). (d) SEM image of a $12 \mu\text{m}^2$ FPI with a center-Ohmic contact (gold, false color) and an additional center-QPC (green, false color) placed along the FPI's edge. An illustration of the edge channels, similar to the one in (c), is provided for $v_B \sim 3$ with the innermost edge channel reflected by center-QPC into the center-Ohmic contact. “Cold” edges, originating from the ground, are not plotted, and arrows represent the current's chirality. Current is impinged on the device from the source side, partitioned at the two QPCs, and probed at the drain side with a cold amplifier. All the three devices (a, b, d) consist of two quantum point contacts,

each with a transmission coefficient controlled by the voltage applied to it ($V_{QPC-left}$ and $V_{QPC-right}$ applied to QPC-left and QPC-right, respectively; see (d)). A charged ‘modulation gate’ (MG) allowed varying the FPI’s area (see SEM images in Fig. 1; blue, false color). Partitioned current is denoted by dashed lines. A modulation-gate (dark blue, false color), biased with the voltage V_{MG} , is employed in all devices in order to modulate the device area.

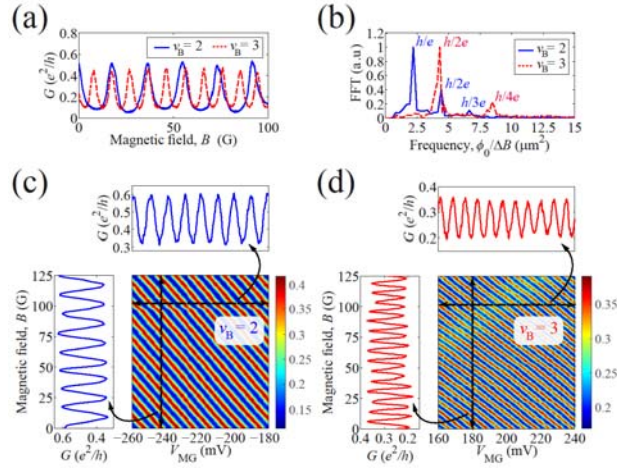


FIG. 2. Aharonov–Bohm interference in the h/e and $h/2e$ regimes measured with a $2 \mu\text{m}^2$ FPI with a grounded center-Ohmic contact. (a) Characteristic AB oscillations with respect to the magnetic field B in the two regimes. (b) Corresponding Fourier transforms; the second harmonic of the h/e periodicity coincides with the first harmonic of the $h/2e$ periodicity. (c, d) Conductance G of the FPI versus both the magnetic field B and the modulation-gate voltage V_{MG} in the h/e regime (c) and in the $h/2e$ regime (d), measured at $B=5.2\text{T}$ ($v_B \sim 2$) and $B=3\text{T}$ ($v_B \sim 3$) respectively.

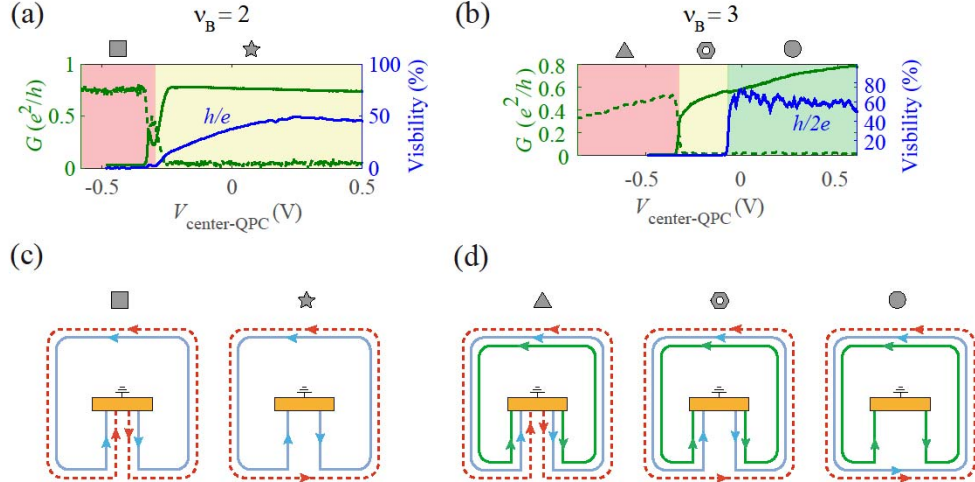


FIG. 3. Grounding edge channels selectively and the effect on interference visibility and conductance. (a, b) Conductance between source and drain through the FPI (green, solid), conductance between source and center Ohmic contact (green, dashed, probed by measuring the voltage across a $1\text{ k}\Omega$ resistor bleeding the current in the center contact to ground) and the visibility of the AB interference of the outermost edge channel (blue) versus the center-QPC voltage $V_{\text{center-QPC}}$. The results at $\nu_B = 2$ are shown in (a), and the results at $\nu_B = 3$ are shown in (b). Regions which differ by the number of fully transmitted channels at center-QPC are marked with different background colors. These regions are illustrated in (c) and (d) for (a) and (b), respectively.

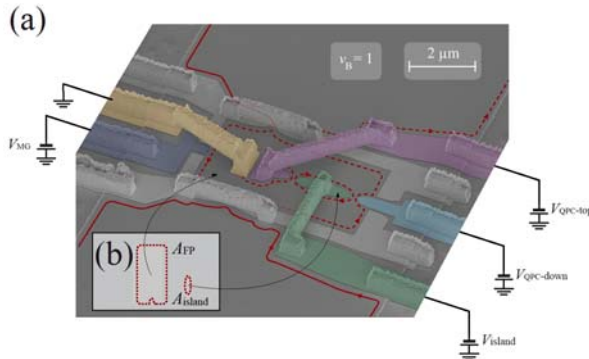


FIG. 4. SEM image of a Fabry-Perot interferometer with an “island” in its center. (a) The FPI shown here is similar to the one in Fig. 1(d), formed by two QPCs, with a modulation-gate (dark blue, false color) and a center Ohmic contact (gold, false color). An additional gate, biased with V_{island} , is placed in the bulk of the interferometer (green, false color). Together with a second gate, placed along the interferometer’s edge (light blue, false color) and biased with V_{down} , it forms QPC-down that allows us to reflect edge channels to the island one by one. With a third gate, placed next to the center Ohmic contact (red, false color) and biased with V_{up} , QPC-up is formed. It allows us to reflect edge channels from the island and into the grounded center Ohmic contact. We denote the area of the interferometer

as A_{FP} , and that of the island as A_{island} . The relevant areas are marked on top of the image with a dashed red line. (b) Inset: another rescaled version of the same areas is shown outside the SEM image for clarity.

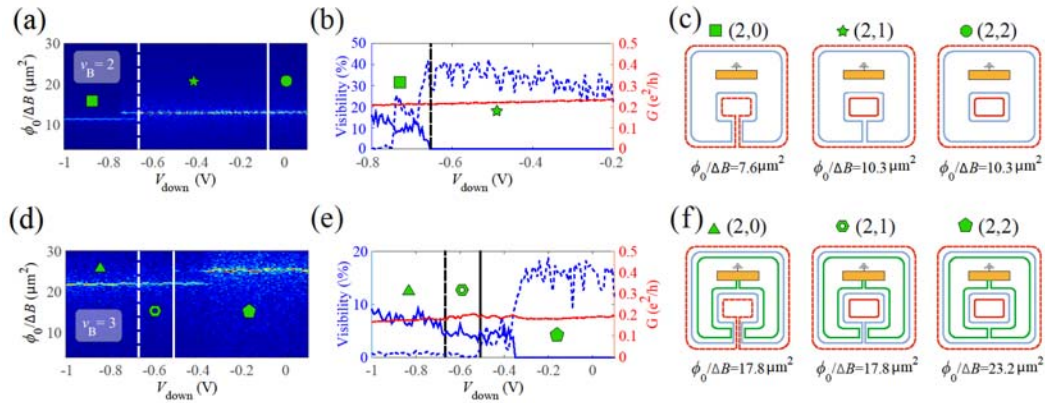


FIG. 5. Evolution of the interference area as QPC-down is pinched, measured with the device in Fig. 4(a). (a) 2D plot of Measurements at $\nu_B = 2$. Each vertical line is the fast Fourier transform of the AB interference oscillations measured as a function of the magnetic field δB for a particular value of V_{down} that determines the transmission of QPC-down. QPC-up is maintained fully open at all times. (b) Conductance (extracted from the AB interference, red) and visibility (extracted from (a), blue) are plotted as functions of V_{down} for fully open QPC-up. (c) Illustrations of different configurations with QPC-down reflecting both edge channels (left), only the outermost edge channel (middle) and none of the edge channels (right). Above each illustration, we show as (ν_{up}, ν_{down}) the numbers of fully transmitted channels in QPC-down, ν_{down} , and in QPC-up, ν_{up} . (d-f) Similar measurements and illustrations as the ones in (a), (b), and (c), respectively, only at $\nu_B = 3$ in the $h/2e$ regime.

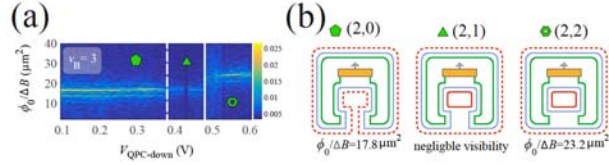


FIG. 6. Evolution of the interference area as QPC-down is pinched, measured with the device in Appendix D at $v_B = 3$. (a) Similar measurement as the ones in Fig. 5(d), taken this time with the device that has extended constriction between the island and the edge of the FPI (see details in Appendix D). (b) Illustrations of different configurations, similar to the ones presented in Fig. 5(f).

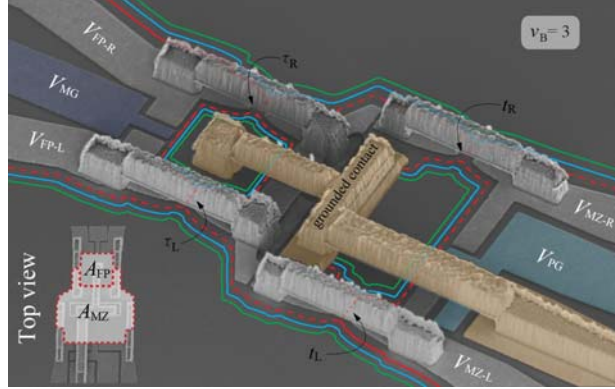


FIG. 7. A Fabry-Perot interferometer on one of a Mach-Zehnder arm. SEM image of the device with an illustration of chiral edge channels at $v_B = 3$. The applied voltages are marked on top of the gates. The modulation gate (V_{MG} , dark blue, false color) is utilized in order to modulate the FPI's. The plunger gate (V_{PG} , light blue, false color), utilized to vary the MZI area. The edge channels are denoted by the colored lines following the edge profile. Dashed lines stand for edge channels that are partitioned at the QPCs. Both Ohmic contacts (gold, false color) in the center of the FPI and on the edge of the MZI are grounded with a common ground. We denote the area of the MZI as A_{MZ} and that of the FPI as A_{FP} , as observed in the top-view SEM image of the device in the inset.

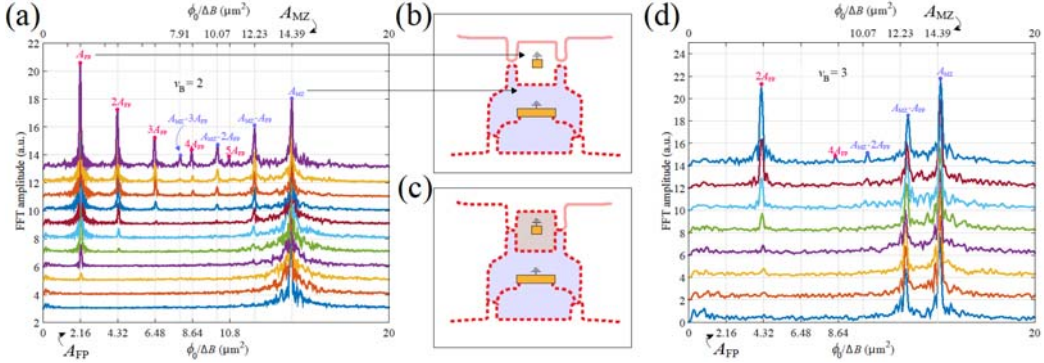


FIG. 8. FFTs of the outermost edge channel's conductance oscillations measured for different configurations of the QPCs of the device seen in Fig. 7. (a) We set both the MZI's and FPI's QPCs to partition the outermost edge channel at $v_B = 2$. While keeping the MZI's QPCs fixed, the transmission of the FPI's QPCs was varied over a wide range. For each value of the FPI QPCs' transmission, we measure interference oscillations as a function of the magnetic field δB and plot its fast Fourier transform from $|t|^2 = 1$ (lowest line, blue) to considerably low transmission (highest line, purple). Both the x -axis above and below the graph denote the frequency in units of μm^2 . The lower axis shows the multiples of the FPI area ($A_{FP}, 2A_{FP}, 3A_{FP}, \dots$), while on the upper axis indicates the combinations of the areas of the MZI and FPI ($A_{MZ} - A_{FP}, A_{MZ} - 2A_{FP}, A_{MZ} - 3A_{FP}, \dots$). (b) An illustration of the device with the QPCs of the MZI partitioning the outermost edge channel, while the QPCs of the FPI are maintained fully open. (c) An illustration of the device with all QPCs partitioning the outermost edge channel. All graphs, except the lowest two, were obtained in that configuration. (d) Similar measurements as shown in (a) at $v_B = 3$ in the $h/2e$ regime.

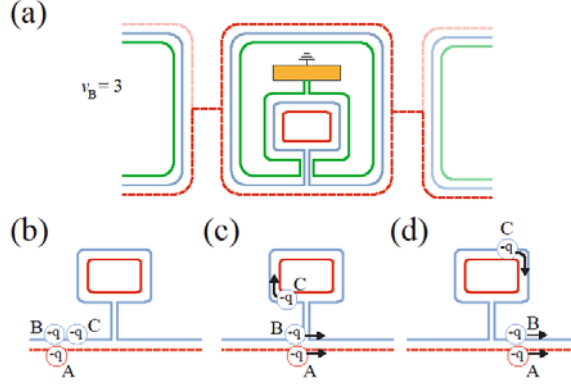


FIG. 9. Schematic representation of neutral mode tunneling at QPC-down. (a) Illustration of the device shown in Fig. 4(a) at $\nu_B = 3$. The semi-transparent lines represent channels at ground or floating channels. The dashed lines represent partitioned current. The configuration illustrated here is the same as the one marked with a hexagon in Fig. 5(f). (b) Negative charge A travels along the chiral outermost channel toward QPC-down. B represents a positive screening charge and C is a compensating negative charge on the neutral inner channel. (c, d) Dipole AB tunnels through the QPC, C continues along the inner channel around the island.